Lattice instability during the martensitic transformation in the high temperature shape memory alloy $\mathrm{Zr(Cu_{0.5}Co_{0.25}Ni_{0.25})}$

M.A. Azeem[a,b,c], D. Dye[a,*]

[a]*Dept. Materials, Royal School of Mines, Imperial College, Prince Consort Road, South Kensington, London SW7 2BP, UK*
[b]*Manchester X-ray Imaging Facility, University of Manchester, Oxford Road, Manchester M13 9PL, UK*
[c]*Research Complex at Harwell, Rutherford Appleton Laboratory, Harwell, Oxfordshire, OX11 0FA, UK*

Abstract

The martensitic transformation on thermal cycling of the polycrystalline $\mathrm{Zr(Cu_{0.5}Co_{0.25}Ni_{0.25})}$ high temperature shape memory alloy was examined using *in situ* synchrotron X-ray diffraction. A single step B2 $\leftrightarrow$ B19′ transformation was observed with a thermal hysteresis of 161 °C and a martensite finish temperature of 294°C. Large anisotropic lattice constrictions and dilations, up to 1.3%, were observed during the course of transformation in the B19′ martensite, but corresponding changes in the B2 austenite were not observed. The coefficients of thermal expansion in both phases were found to be quite large, 33×10^{-6} °C^{-1} in B2 and ~~$29 — 88 \times 10^{-6}$ °C^{-1} for a_{B19′} — c_{B19′}~~ 39, 88 and 29×10^{-6} °C^{-1} for $a_{B19′}$, $b_{B19′}$ and $c_{B19′}$ respectively. Possible mechanisms governing the transformation behaviour are discussed.

Keywords: Shape memory; Intermetallics; x-ray diffration, synchrotron radiation

1. Introduction

Shape memory functionality in intermetallic alloys based on NiTi and $\mathrm{Ni_2MnGa}$ is realised by the exploitation of a diffusionless transformation from one crystal structure to another on changes in temperature, stress state and, in some alloys, under the influence of magnetic field. Usually, the high temperature (austenite) phase has high symmetry and on cooling it shears into twin-related variants of the product low symmetry, low temperature (martensite) phase. The loading of martensite at low temperatures results in the observation of a stress plateau associated with detwinning; the loading of austenite just above

---

the thermal transformation results in the observation of a plateau associated with stress-induced transformation.

The presence of a bias stress during thermal cycling allows a degree of variant selection to occur, a phenomenon that may also be induced by the presence of nucleating intermetallics or by cold working to engineer the grain boundary and defect state. Typically, the transformation progresses gradually and a hysteresis is observed which is attributed to the energy dissipated in moving the austenite/martensite interfaces [1, 2, 3] which is in turn related to the availability of variants, self accommodation [4] and the interface strains that result in the generation of interface defects [5].

Shape memory alloys (SMAs) are used or suggested for a wide variety of applications that exploit different attributes of the shape memory functionality. Austenitic seismic dampers [6] use transformation in each load cycle, making use of the large recoverable strain and hysteresis gained during stress induced transformation. In contrast, martensitic shape memory materials detwin at low temperatures and then recover the shape on heating; this is the phenomenon used in arterial stents [7]. NiTi wires have been demonstrated to actuate bistable air flow structures such as doors and air inlets in aircraft engines and other propulsion systems [8] using thermal actuation. Recently, bimetallic NiTi / Ti thermal actuators have been suggested for noise control in gas turbine variable area nozzles [8, 9, 10]. This leads to the suggestion that high temperature shape memory alloys (HTSMAs) could be used for airflow control elsewhere in gas turbines [11]. However, having a detailed understanding of the micromechanics of the transformations become more critical as multi-cycle, structural and more safety-critical components are suggested.

Most HTSMAs are ternary or quaternary alloys based on binary alloy systems. For example, NiTi based HTSMAs can be designed by the stoichiometric replacement of Ti by Zr and Hf [12, 13, 14] or the replacement of Ni by Pd [15, 16, 2], Pt [15] or Au [15]. The transformation temperatures of the resulting alloys depend on the element(s) used and the extent of alloying. Apart from transformation temperatures, SMAs may therefore be further classified based on the solubility limit of alloying elements. For example, in case of NiTi based alloys Pd could completely replace Ni and form a very high temperature equiatomic PdTi alloy, whilst only $\approx$20 at.% Ti can be replaced by Hf, Zr or Hf+Zr. The transformation temperatures of the NiTi based HTSMAs range from 100 °C to 900 °C but only a maximum of $\approx$ 300 °C has been achieved without using high density and expensive additions like Pd, Pt and Au [12].

ZrCu based HTSMAs may be attractive alternatives to NiTi in terms of the maximum transformation temperatures and the economical alloying possibilities. The transformation temperatures of $Zr_{50}Cu_{25}Co_{25-X}Ni_X$ alloys increase with Ni content, with a maximum transformation temperature of $\approx$ 750 °C achieved in the end-member $Zr_{50}Cu_{25}Ni_{25}$ alloy [17]. In contrast, $Zr_{50}Cu_{25}Co_{25}$ undergoes transformation in the vicinity of room temperature. Both equiatomic binary ZrCu and $Zr_{50}Cu_{25}Co_{25}$ are reported to be brittle, but the addition of Ni improves ductility [18]. Ni contents > 15 at.% stabilize a martensite with the centered monoclinic (Cm space group) crystal structure instead of the con-

ventional B19′ martensite [17]. The Cm phase in Zr intermetallics was first reported in binary ZrCu [17, 19] and is observed to be present to some extent in all ZrCu based alloys.

For efficient and reliable actuator design it is essential that the transformation temperatures and strains are stable in service. In SMAs the functionality depends on variant selection which is the product of self accommodation [4], the interface energy [2] and the defect concentration. These in turn are interdependent and related to the local stress states within each grain, and to the material history. For example, the interface stresses depend on the difference in moduli and the misfit between the participating phases and the overall defect concentration depends on many factors including dislocation adsorption into growing twin boundaries. Crystallographic variants for a given set of phase candidates in a martensitic transformation can be predicted using the phenomenological theory of martensitic transformations (PTMT) [20]. This approach, in tandem with a combinatorial search [21, 22] can be used to identify stable SMAs with minimum thermal hysteresis [21].

SMAs are commonly characterised using bulk thermodynamic techniques such as calorimetry, dilatometry and resistivity, which do not reveal the evolution of crystallography-specific information. In situ transmission electron microscopy (TEM) can be used, but it cannot be directly correlated to the bulk behaviour because of the lack of constraint in thin films – for example, the transformation temperatures are commonly found to be quite different. For some combinatorial approaches using thin film deposition, this may be a limitation.

In the present paper, we use *in situ* synchrotron X-ray diffraction (sXRD) to examine a polysrystalline $Zr_{50}Cu_{25}Co_{12.5}Ni_{12.5}$ alloy. This approach allows crystallographic information to be obtained whilst retaining stress states representative of real actuators. As an initial exploration of this candidate HTSMA system we focus on the behaviour of a single alloy which offers conventional B2 (austenite) ↔ B19′ transformation behaviour (low Ni content). The alloy chosen aims to avoid the intrinsic brittleness of $Zr(Cu_{0.5}Co_{0.5})$, in the anticipation that should this system prove promising then hysteresis minimisation will be possible using the PTMT approach in combination with Vegard's Law [23].

2. Experimental

[Figure 1 about here.]

The alloy was prepared by vacuum arc melting using pure elemental Zr, Cu, Co and Ni in a pressure controlled pure Ar environment. The elements used were in lump form with a maximum dimension below 5 mm and very fine particles were avoided to eliminate elemental loss due to arc force during melting. A ∼ 60 g ingot was prepared by melting and remelting with intermittent flipping to minimise elemental segregation. The ingot was encapsulated in quartz tube and homogenised at 800 °C for 24 h, re-encapsulated in a steel can with commercially pure Ti powder to provide the necessary thermal insulation and

3

lateral constraint to minimise cracking and then hot rolled to 80% strain at 800 °C with 5 min interpass annealing. Sufficient plastic deformation from a process like rolling is necessary to produce recrystallisation in order to produce a fine enough grain size to observe complete Debye-Scherrer rings in diffraction, Figure 1a. The grain size was found to be ~ 30 μm. Initial estimates of the transformation temperatures were obtained by calorimetry using a Mettler Toledo 822^e DSC. Flat dog-bone specimens with a $0.5 \times 0.5 \times 30$ mm gauge length were fabricated electro-discharge machining and grinding. The specimen was then thermally cycled at a rate of 2 $°Cs^{-1}$ with a constant load of 5 MPa using an Instron electro-thermo mechanical testing machine (ETMT) at the ID15B powder diffraction beamline at the ESRF, Grenoble, France. A monochromatic beam of 0.5×0.5 mm with a wavelength of 0.1427 Å was used and complete Debye-Scherrer rings recorded using a Thales Pixium 4700 detector [33] mounted at a distance of 1.228 m from the sample, Figure 1b. The instrument parameters were determined using a LaB_6 calibration powder in a glass capillary. The temperature of the specimen was measured by an R-type thermocouple placed immediately above the diffracting volume. The position of thermocouple also facilitated in identifying the central gauge volume to a precision of 0.1 mm. This was necessary in order for the maxima in temperature produced by the quadratic temperature profile along the gauge length from resistance heating using water-cooled grips to be placed at the control thermocouple location.

3. Results

Broad area EDX analysis in the SEM was used to verify the composition; the matrix was found to be Zr rich, Table 1. The variation in composition observed is a consequence not only of the uncertain in EDX, which is on order of 1 at.%, but also incomplete homogenisation of the solidification segregation. The use of a higher homogenisation temperature was not possible, as it would have been above the melting point, and therefore it is felt likely that solidification segregation will remain a challenge in this alloy. Rietveld refinement [24] of the whole-ring diffraction patterns was used to obtain the phase fractions and lattice parameters, using the generalised structural analysis package (GSAS) [34, 35] and the area detector analysis package Fit2D [36]. sXRD thermal cycling experiments were performed on an unstressed sample in transmission mode using resistive heating. The room temperature (martensitic) diffraction patterns and those from first heating into the austenite phase are shown in Figure 2. The lattice parameters and phase fractions were obtained using Reitveld refinement [24]; a spherical harmonic texture model [25] was used to account for the rolling texture.

[Table 1 about here.]

[Figure 2 about here.]

4

In a powder diffraction pattern, the Debye – Scherrer rings do not remain circular when there are orientation-dependent stresses in the sample. In the current case, the peak positions were not found to vary with azimuthal angle, Figure 3, although intensity variations associated with the rolling texture were observed. Therefore, in the remainder of the analysis presented here, whole ring integrations have been used.

[Figure 3 about here.]

[Figure 4 about here.]

The evolution of the diffraction patterns on thermal cycling in the region around the {110} B2 peak is shown in Figure 4. The transformation from $P2_1/m$ B19$'$ to $Pm\bar{3}m$ B2 first begins at around 475°C and completes at around 570°C. In the high temperature state, it is clear that a small amount of Cm phase remains, possibly accompanied by another intermetallic phase. On cooling, the (111) and (002) B19$'$ peaks broaden and merge. This is also visible in Figure 3(a) and (d). For long term cyclic stability it is desirable for an SMA to undergo complete transformation from one phase to another but in reality a small amount of low temperature martensite remains untransformed in the microstructure on heating above the austenite finish temperature (A_f) [26] and *vice-versa* on cooling below the martensite finish temperature (M_f) [16, 2]. This presence of retained austenite in between growing martensite variant groups is expected to be due to the stress stabilisation of the austenite by the transformation strains [2]. In the current alloy the amount of retained martensite is slightly higher than that observed in Zr- and Hf- containing NiTi based HTSMAs [27, 28].

[Figure 5 about here.]

[Table 2 about here.]

Although the martensite finish (M_f) temperature in the current alloy is very high, the overall transformation occurs over a wider temperature range, Figure 5 and Table 2, than the more commonly known NiTi based HTSMAs [27, 29]. The peak transformation temperatures, A_p and M_p corresponding to 50% martensite on heating and cooling are observed to be 498 and 337°C respectively. Therefore the peak transformation hysteresis (A_p-M_p) in the current alloy is 161 °C, about 3.5 to 6× larger than in NiTi [3] and $\approx$ 2.7× larger than in the $Ni_{50}Ti_{35}Hf_{15}$ [27, 28, 29]. The forward B19$'$ to B2 transformation occurs over a wider temperature range than the reverse transformation during cooling. For example, the transition from 80 to 10 % martensite during heating in cycle 5 occurs over 96 °C while on cooling this occurs over 58 °C. Further, the final dissolution from $\approx$20 to 5% martensite in each heating cycle occurs over a greater temperature range than initial re-precipitation on cooling. The start and finish transformation temperatures have been evaluated by applying a martensite volume fraction cut off limit of 80% for A_s and M_f and similarly

5

a 10% limit has been used for A_f and M_s; the transformation temperatures for all five thermal cycles thus evaluated are listed in Table 2. A_s and A_f for the first heating cycle are ≈ 60 °C higher than the corresponding temperatures in the rest of the cycles; however, a similar difference was not observed for M_s and M_f.

Figure 5 shows the evolution of the lattice parameters of the phases and the corresponding unit cell volumes in the alloy before inception and during the course of transformation during the first, second and fifth thermal cycles. The lattice parameters of the B19′ at room temperature and the B2 at 620 °C are provided in Table 3 along with those for the B2 and B19′ in binary near-equiatomic NiTi [30] and ZrCu [31]. Clearly, the B19′ unit cell in the current alloy is larger than in NiTi and ZrCu and the B2 is $\approx 0.4\%$ larger than in NiTi.

[Table 3 about here.]

Because the monoclinic cell has two-fold centrosymmetry, thermal expansion C_T can only be uniquely described by the variation in a, b, c and γ, Table 3. Compared to conventional metals, both phases have quite high thermal expansion. In particular, it is very large for $b_{B19'}$, at 88.2×10^{-6} °C^{-1}, and the monoclinic shear angle γ is strongly temperature dependent. This is probably best understood in terms of the high vibrational entropy (and soft phonons) of crystal structures associated with shear transformations.

Complete recovery is observed at the end of every thermal cycle in each of the B19′ and B2 lattice parameters except the monoclinic angle γ which undergoes a permanent change of $0.11°$ (from $103.23°$ to $103.34°$ or 0.1%) on cooling at the end of the first thermal cycle, but subsequently stabilises. Such per-cycle evolution was observed to be much more prominent in NiTi based HTSMAs [27, 28].

It is instructive to compare the B2 and B19′ lattice parameters. $\sqrt{2}a_{B2} = 4.603$ Å is nominally equivalent to $b_{B19'}$ and $c_{B19'}$, which in fact are around $\pm 10\%$ larger / smaller, which is similar in magnitude to the net shear of $12.7°$; the volume change is less than 1%. During the course of the heating transformation, very large decreases in the B19′ lattice parameters are observed, Table 3 (denoted 'strain') and Figure 5; for example, $a_{B19'}$ changes by -0.34% during the course of the transformation. These changes are *not* orientation-dependent; an analysis of different ring segments produces the same result, which suggests that they are not the result of accommodation stresses [27]. In the case of $a_{B19'}$ and $c_{B19'}$, these changes are away from the ideal B2 orientation relationship; that is, these are not gradual moves to and from the B2 structure.

The reverse changes are observed on cooling, and at maximum, these strains are equivalent to a 2% dilatation. Also, $a_{B19'}$ and $\gamma_{B19'}$ then rise at the very end of the heating transformation. Finally, before transformation begins, $b_{B19'}$ and $\gamma_{B19'}$ undergo a cessation of thermal expansion, although this is small compared to the subsequent changes during transformation; this interruption is confined to the heating transformation.

In complete contrast, no such large deviations are observed in the B2 phase on transformation.

6

[Figure 6 about here.]

Figure 6 shows the measured sample dilatations. Because resistance heating was used, which preferentially heats the central region where the diffraction beam and thermocouple were co-located, these dilatations and constrictions cannot be directly converted to strain. However, they do indicate the macroscopic hysteresis observed in the sample and overall changes in specimen length at the ends of transformation. It is observed that the sample gradually extended over the five thermal cycles utilised, in common with most SMAs. In agreement with the diffraction results, they also indicate that A_f remained constant during cycles 2-5, but with a large change between cycles 1 and 2. In contrast, M_s and M_f remained fairly constant (again, consistent with the diffraction results), as did the actuator position at the end of the heating ramp.

4. Discussion

In the experiments performed here, the martensite transformation on cooling did not complete at the end of each thermal cycle; however the on-heating austenite transformation did complete each time. The results are consistent with recovery of the same parent 100% austenite grain structure at the end of each heating cycle. Therefore the lack of evolution in cycles 2-5 usually observed in SMAs possessing hysteresis is presumably due to the transformation not being run to complete dissolution of the austenite on cooling. However, that does not prevent the sample from gradually extending on thermal cycling, which is most likely, from an examination of the diffraction patterns, to be due to a gradual variant selection process operating in the B19′ phase.

The major challenge in interpreting the results observed here is understanding the lattice parameter changes that occur in the B19′ on heating. Because the B19′ – B2 interfaces are believed to be sharp [2] then for alloys where $\lambda_2 \neq 1$, *i.e.* with non-zero distortion on the interface plane (the present case), the large interface strains must be accommodated by interface defects. However, one can examine the present data against the following hypotheses - (i) that the changes are due to accommodation stresses between the laths and the B2, (ii) that they are a product of the defect configurations and martensite lath widths, (iii) that they are associated with physical changes in the crystal behaviours at the point of marginal stability. Zener [32] pointed out that crystals at the limit of stability must have near-zero shear moduli in the shearing directions. Therefore, these large strains might be a general feature of martensitic transformations.

The lattice parameter changes are observed in different ring segments as well as the entire-ring integrations presented here, which in the rolled sheet employed here would tend to suggest that the effect is not related to the specimen texture and therefore, to variant accommodation mechanisms. In addition, the volume change observed would mitigate against a variant accommodation stress mechanism, as would the lack of corresponding deviations in the B2. However, not all the lattice parameter changes in the B19′ (e.g. $\gamma_{B19'}$) are towards the B2 structure, and nor does the B2 show changes during the transformation;

both of these observations suggest that hypothesis (iii) cannot be a complete explanation.

The lattice parameter changes observed, if interpreted as strains, are quite large, on the order of 1%. The first martensite to appear would be heavily constrained by the surrounding B2 but as it grew could relax increasing amounts of stress by the growth of adjacent variants; this could plausibly generate strains on the order of 1%, which is similar in magnitude to the yield strain of detwinned martensite. This line of reasoning does not, however, explain the minima observed in $a_{B19'}$ and $\gamma_{B19'}$ on heating only, and orientation independence. However, this occurs towards the end of transformation, when the austenite ribs between the B19′ laths become thick enough to link up and for any variant accommodation effects to therefore cease to apply. At this point, interface defect effects may become dominant.

It is interesting to interpret these issues in relation to the phenomenological theory of martensite transformations. The special case where the interface strain is zero, $\lambda_2 = 1$, has been shown to be a criterion that minimises hysteresis [21], and in this case no interface defects will be produced and the elastic strains associated with martensite precipitation will be zero. However, far from this condition, as in the present case, an elastic analysis inspired by this approach will fail as interface defects and any associated anisotropy and stress fields will need to be accounted for.

5. Conclusions

The transformation behaviour of polycrystalline $Zr(Cu_{0.5}Co_{0.25}Ni_{0.25})$ has been examined using synchrotron X-ray diffraction. The following conclusions can be drawn

- The alloy is a plausible candidate high temperature shape memory alloy, with a stabilised martensite finish temperature of 294 °C, but has a high hysteresis of around 161 °C.

- The alloy can be produced in a polycrystalline form and was found to be ductile.

- The thermal expansion coefficients were found to be quite large in both phases, 33×10^{-6} °C^{-1} for the B2 and from 29–88 $\times 10^{-6}$ °C^{-1} for $a_{B19'} - c_{B19'}$.

- Large deviations in the B19′ lattice parameters, up to1.25%, are observed during the transformation and particularly on heating. In contrast, the B2 lattice parameters remain undisturbed.

The mechanism of these deviations is not completely clear; however, the minima observed, the direction of the deviations away from the B2 ideal orientation relationship and the lack of mirroring deviations in the B2 all suggest that they cannot solely be due to elastic variant accommodation effects and that interface defects will also be a part of any complete explanation.

References

[1] R. Zarnetta, A. Savan, S. Thienhaus, and A. Ludwig, "Combinatorial study of phase transformation characteristics of a Ti–Ni–Pd shape memory thin film composition spread in view of microactuator applications," *Applied Surface Science*, vol. 254, pp. 743–748, Nov. 2007.

[2] R. Delville, S. Kasinathan, Z. Zhang, J. Van Humbeeck, R. D. James, and D. Schryvers, "Transmission electron microscopy study of phase compatibility in low hysteresis shape memory alloys," *Philosophical Magazine*, vol. 90, no. 1-4, pp. 177–195, 2010.

[3] R. Zarnetta, R. Takahashi, M. L. Young, A. Savan, Y. Furuya, S. Thienhaus, B. Maass, M. Rahim, H. Brunken, Y. S. Chu, V. Srivastava, R. D. James, I. Takeuchi, and A. Ludwig, "Identification of Quaternary Shape Memory Alloys with Near-Zero Thermal Hysteresis and Unprecedented Functional Stability," *Advanced Functional Materials*, vol. 20, no. 12, pp. 1917–1923, 2010.

[4] K. Madangopal, "The self accommodating martensitic microstructure of NiTi shape memory alloys," *Acta Materialia*, vol. 45, pp. 5347–5365, Dec. 1997.

[5] R. C. Pond, S. Celotto, and J. P. Hirth, "A comparison of the phenomenological theory of martensitic transformations with a model based on interfacial defects," *Acta Materialia*, vol. 51, no. 18, pp. 5385–5398, 2003.

[6] M. Dolce and D. Cardone, "Mechanical behaviour of shape memory alloys for seismic applications 1. Martensite and austenite NiTi bars subjected to torsion," *International Journal of Mechanical Sciences*, vol. 43, no. 11, pp. 2631–2656, 2001.

[7] T. Duerig, A. Pelton, and D. Stöckel, "An overview of nitinol medical applications," *Materials Science and Engineering A*, vol. 273-275, pp. 149–160, 1999.

[8] D. J. Hartl and D. C. Lagoudas, "Aerospace applications of shape memory alloys," *Proceedings Of The Institution Of Mechanical Engineers Part G-Journal Of Aerospace Engineering*, vol. 221, no. G4, pp. 535–552, 2007.

[9] N. T. Birch and J. R. Webster, "Gas turbine engine exhaust nozzle having a noise attenuation device driven by shape memory material actuators," US Patent US7000378, Feb. 2006.

[10] F. T. Calkins, J. H. Mabe, and G. W. Butler, "Boeing's variable geometry chevron: morphing aerospace structures for jet noise reduction," in *Proc. SPIE*, p. 61710O, SPIE, 2006.

[11] J. Webster, "High integrity adaptive SMA components for gas turbine applications," in *Proc. SPIE*, p. 61710F, SPIE, 2006.

[12] J. H. Mulder, *Investigation of high temperature shape memory alloys from the Ni-Ti-Zr and Ni-Ti-Hf systems.* PhD thesis, University of Twente, Twente University, 1995.

[13] J. Van Humbeeck, "High Temperature Shape Memory Alloys," *Journal of Engineering Materials and Technology*, vol. 121, no. 1, pp. 98–101, 1999.

[14] G. S. Firstov, J. Van Humbeeck, and Y. N. Koval, "Comparison of high temperature shape memory behaviour for ZrCu-based, Ti–Ni–Zr and Ti–Ni–Hf alloys," *Scripta Materialia*, vol. 50, pp. 243–248, Jan. 2004.

[15] P. M. Huisman-Kleinherenbrnik, *On the martensitic transformation temperatures in NiTi and their dependence on alloying elements.* PhD thesis, University of Twente, University of Twente, 1991.

[16] R. Delville, D. Schryvers, Z. Zhang, and R. D. James, "Transmission electron microscopy investigation of microstructures in low-hysteresis alloys with special lattice parameters," *Scripta Materialia*, vol. 60, no. 5, pp. 293–296, 2009.

[17] G. S. Firstov, Y. N. Koval, and J. Van Humbeeck, "Irreversible Processes During Martensitic Transformation in Zr-Based Shape Memory Alloys," *J. Phys. IV, Proc. (France)*, vol. 07, pp. 549–554, Nov. 1997.

[18] Y. N. Koval, G. S. Firstov, L. Delaey, and J. V. Humbeeck, "The influence of Ni and Ti on the martensitic transformation and shape memory effect of the intermetallic compound ZrCu," *Scripta Metallurgica et Materialia; (United States)*, vol. 31, pp. 799–802, Oct. 1994.

[19] J. W. Seo and D. Schryvers, "Defect structures in CuZr martensite, studies by CTEM and HRTEM," *Journal De Physique Iv*, vol. 7, no. C5, pp. 149–154, 1997.

[20] D. S. Lieberman, M. S. Wechsler, and T. A. Read, "Cubic to orthorhombic diffusionless phase change – Experimental and theoretical studies of AuCd," *Journal of Applied Physics*, vol. 26, no. 4, pp. 473–484, 1955.

[21] J. Cui, Y. S. Chu, O. O. Famodu, Y. Furuya, J. Hattrick-Simpers, R. D. James, A. Ludwig, S. Thienhaus, M. Wuttig, Z. Y. Zhang, and I. Takeuchi, "Combinatorial search of thermoelastic shape-memory alloys with extremely small hysteresis width," *Nature Materials*, vol. 5, no. 4, pp. 286–290, 2006.

[22] V. Shastry, V. Divya, M.A. Azeem, A. Paul, D. Dye, and U. Ramamurty, "Combining indentation and diffusion couple techniques for combinatorial discovery of high temperature shape memory alloys," *Acta Materialia*, vol. 61, no. 15, pp. 5735 – 5742, 2013.

[23] L. Vegard, "Die Konstitution der Mischkristalle und die Raumfüllung der Atome," *Zeitschrift für Physik A Hadrons and Nuclei*, vol. 5, pp. 17–26, 1921.

[24] H. M. Rietveld, "A profile refinement method for nuclear and magnetic structures," *J Appl Crystallography*, vol. 2, pp. 65–71, June 1969.

[25] H. Sitepu, W. W. Schmahl, and R. B. Von Dreele, "Use of the generalized spherical harmonic model for describing crystallographic texture in polycrystalline NiTi shape-memory alloy with time-of-flight neutron powder diffraction data," *Applied Physics A: Materials Science & Processing*, vol. 74, pp. S1676–S1678, 2002.

[26] R. Basu, L. Jain, B. Maji, M. Krishnan, K. Mani Krishna, I. Samajdar, and P. Pant, "Origin of Microstructural Irreversibility in Ni-Ti Based Shape Memory Alloys during Thermal Cycling," *Metallurgical and Materials Transactions A*, vol. 43, no. 4, pp. 1277–1287, 2012.

[27] M.A. Azeem, *Diffraction investigations of high temperature shape memory alloys*. PhD thesis, Imperial College London, United Kingdom, 2013.

[28] M.A. Azeem and D. Dye, "In situ evaluation of the transformation behaviour of niti-based high temperature shape memory alloys," *Intermetallics*, vol. 46, pp. 222 – 230, 2013.

[29] X. L. Meng, Y. X. Tong, K. T. Lau, W. Cai, and L. M. Zhou, "Effect of Cu addition on phase transformation of Ti-Ni-Hf high-temperature shape memory alloys," *Materials Letters*, vol. 57, no. 2, pp. 452–456, 2002.

[30] N. G. Jones and D. Dye, "Martensite evolution in a NiTi shape memory alloy when thermal cycling under an applied load," *Intermetallics*, vol. 19, pp. 1348–1358, Oct. 2011.

[31] D. Schryvers, G. S. Firstov, J. W. Seo, J. Van Humbeeck, and Y. N. Koval, "Unit cell determination in CuZr martensite by electron microscopy and X-ray diffraction," *Scripta Materialia*, vol. 36, no. 10, pp. 1119–1125, 1997.

[32] C. Zener, "Elasticity and anelasticity of metals," p. 170, University of Chicago Press, 1948.

[33] J. E. Daniels and M. Drakopoulos, "High-energy X-ray diffraction using the Pixium 4700 flat-panel detector," *Journal of Synchrotron Radiation*, vol. 16, pp. 463–468, May 2009.

[34] B. H. Toby, "EXPGUI, a graphical user interface for GSAS," *Journal Of Applied Crystallography*, vol. 34, pp. 210–213, 2001.

[35] A. C. Larson and R. B. Von Dreele, "GSAS: general structure analysis system," *Report LAUR 86-748*, 1994.

[36] A. P. Hammersley, S. O. Svensson, M. Hanfland, A. N. Fitch, and D. Hausermann, "Two-dimensional detector software: From real detector to idealised image or two-theta scan," *High Pressure Research*, vol. 14, pp. 235–248, Jan. 1996.

Table 1: Composition (at.%) of the alloy measured using Energy Dispersive X-ray (EDX) Spectroscopy.

	Zr	Cu	Co	Ni
Minimum	50.6	20.6	8.3	8.7
Maximum	58.3	24.8	13.1	13.6
Mean	56.2	22.6	9.7	11.5
Standard Deviation	1.9	1.1	1.3	1.1

Table 2: Transformation temperatures for all five thermal cycles (C1–C5) in °C. 80% volume fraction martensite was used as cut off limit for A_s and M_f and 10% was used for A_f and M_s.

	C1	C2	C3	C4	C5
Austenite start, A_s	488	421	420	420	419
Austenite finish, A_f	576	523	522	525	522
Martensite start, M_s	357	355	354	354	355
Martensite finish, M_f	296	295	295	294	294

Table 3: Coefficients of thermal expansion, C_T, Rietveld refined lattice parameters of the B2 and B19′ at 620 °C and room temperature respectively, along with the maximum transformation induced change (Δ) and the corresponding strain along the crystallographic axes of the two phases during transformation. Lattice parameters of B19′ and B2 in NiTi [30] and ZrCu [31] are provided for comparison. Uncertainties for the current alloy are in parenthesis and for NiTi they are reported to be of the order of $\approx 10^{-3}$ [30]. Lengths are in Å, B19′ unit cell angle is in ° and the unit cell volume is in Å^3.

	ZrCu	$Zr(Cu_{0.5}Co_{0.25}Ni_{0.25})$	NiTi	C_T $\times 10^{-6}\,°C^{-1}$	Δ	strain %
$a_{B19'}$	3.2	3.2688(6)	2.90	39.2(3)	-0.011	-0.34
$b_{B19'}$	5.2	5.1181(9)	4.65	88.2(9)	-0.044	-0.85
$c_{B19'}$	3.9	4.1913(7)	4.12	29.3(5)	-0.052	-1.25
$\gamma_{B19'}$	106	102.75(2)	97.5	1770(20)	-0.350	-0.34
a_{B2}	–	3.25489(7)	3.02	33.4(4)	-0.0005	-0.02
$V_{B19'}$	–	68.39(2)	–	–	-1.402	-2.05
$2V_{B2}$	–	69.036(4)	–	–	-0.04	-0.05

(a)

Azimuthal angle (ψ)

(b) Pixium 4700 detector

Diffracted beam

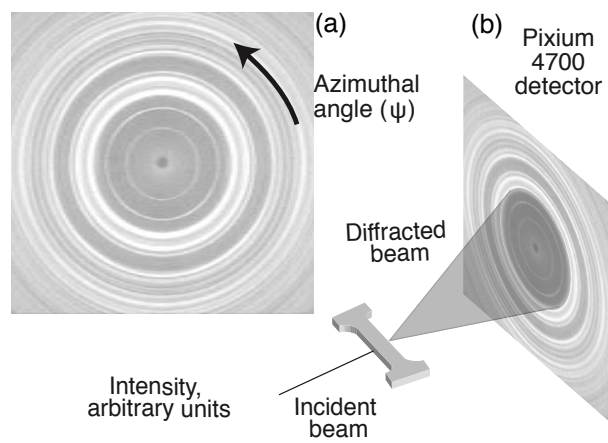Intensity, arbitrary units

Incident beam

Figure 1: (a) Complete Debye-Scherrer rings from monoclinic martensite and (a) schematic of the synchrotron X-ray diffraction setup
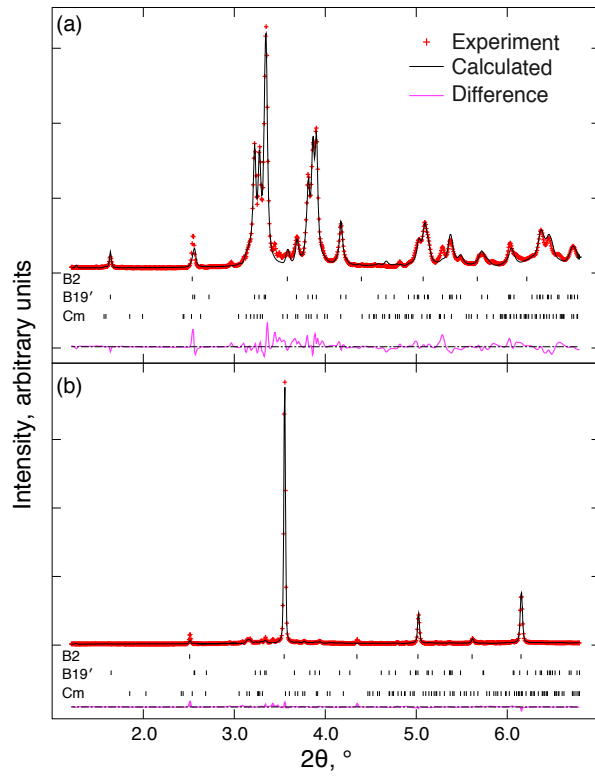
Figure 2: Diffraction spectra obtained from full-ring integration of 2D area detector data obtained during monochromatic high energy transmission X-ray diffraction of $Zr_{50}Cu_{25}Co_{12.5}Ni_{12.5}$ (a) in the low temperature monoclinic martensite state and (b) in the high temperature cubic austenite state. In both cases a small amount of the Cm phase is observed.
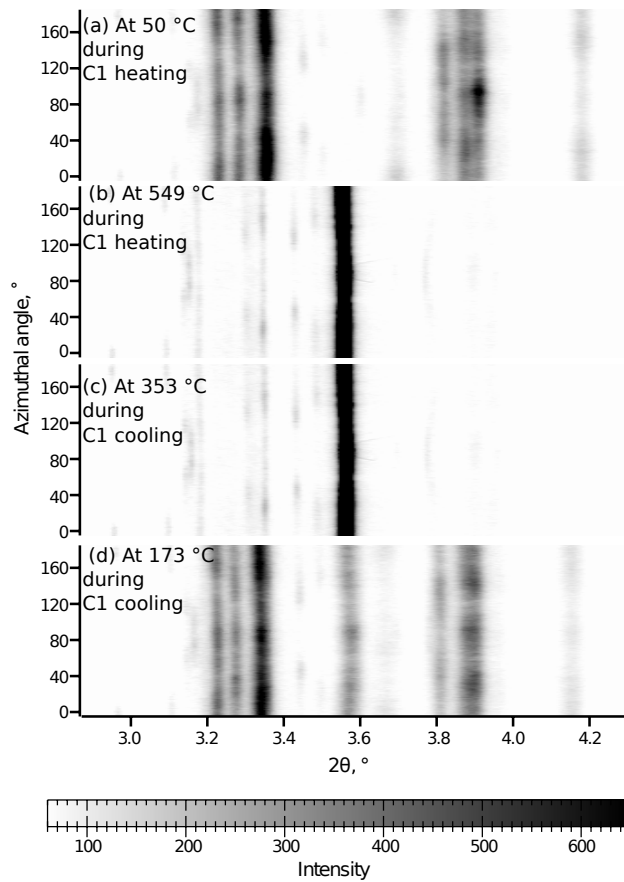
Figure 3: Evolution (a-d) of the diffraction rings during the first thermal cycle, C1, with azimuthal angle. No observable variation in diffraction angle with orientation is observed, although intensity variations associated with the texture can be readily seen.
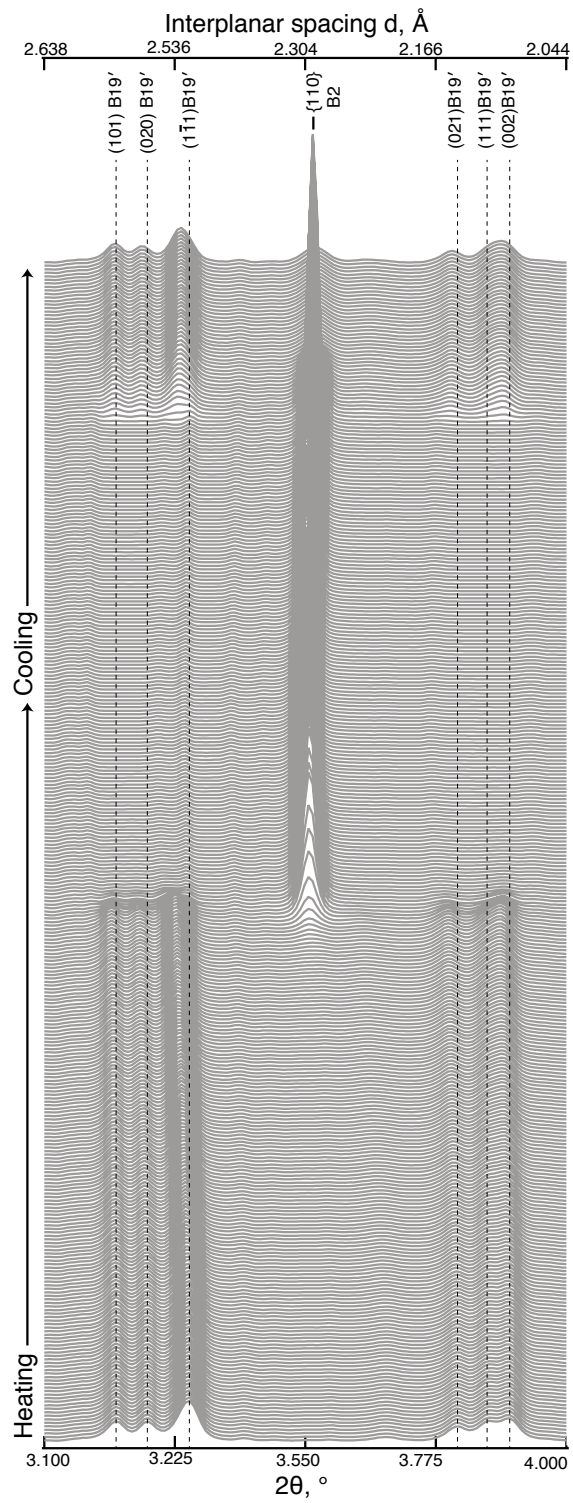
18

Figure 4: Evolution during the first thermal cycle in $Zr_{50}Cu_{25}Co_{12.5}Ni_{12.5}$ around the {110} B2 peak.
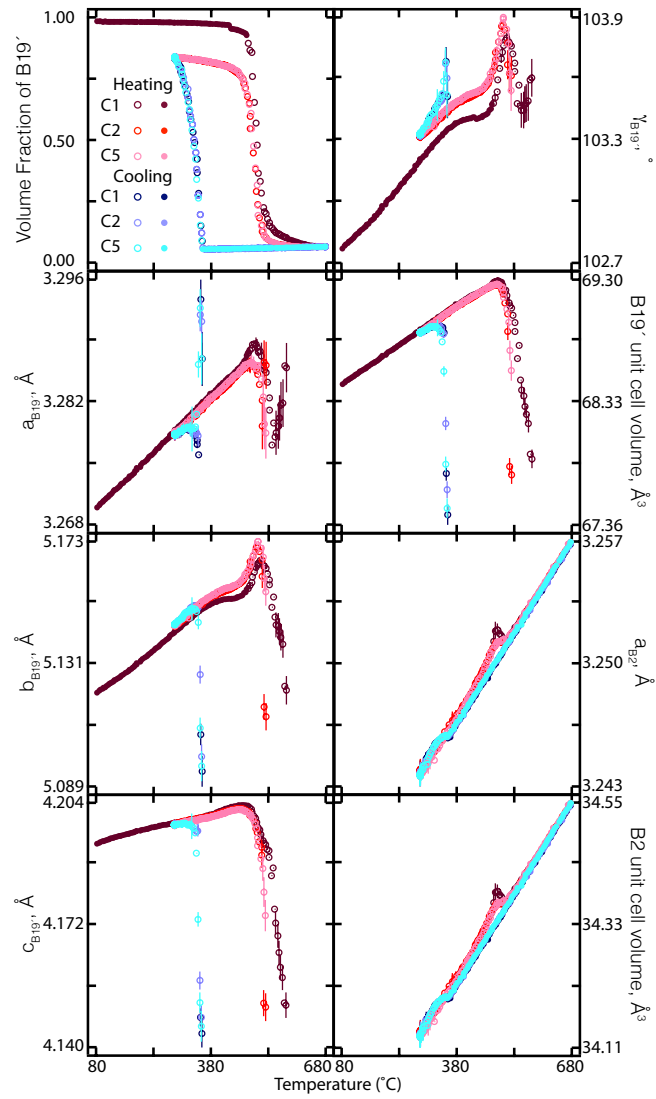
Figure 5: Monoclinic martensite and cubic austenite unit cell evolution evaluated as a function of specimen temperature. Solid symbols are in the single phase region and open symbols are shown during transformation. Cn refers to the cycle number.
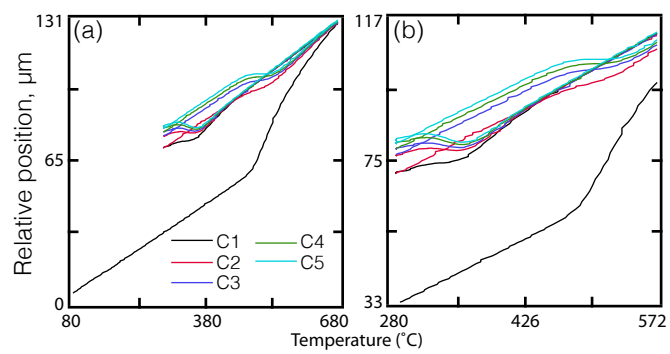
20

Figure 6: Overall actuator motion measured from the thermo-mechanical testing machine during transformation, (a) over the entire testing range and (b) in the vicinity of transformation.

21